

M O enes family materials with Dirac nodal loop, strong light-harvesting ability, long carrier lifetime and conduction-band valley spin splitting

Luo Yan,^{1,*} Junchi Liu,² Yu-Feng Ding,¹ Jiafang Wu,³ Bao-Tian Wang,⁴ Hao Gao,⁵ and Liujiang Zhou^{2,†}

¹*School of Mathematics and Physics, University of South China, Hengyang 421001, China*

²*School of Physics, University of Electronic Science and Technology of China, Chengdu 610054, China*

³*College of Physics and Engineering, Chengdu Normal University, Chengdu, 611130, China*

⁴*Institute of High Energy Physics, Chinese Academy of Science (CAS), Beijing 100049, China*

⁵*Fritz-Haber-Institut der Max-Planck-Gesellschaft, Faradayweg 4-6, 14195 Berlin, Germany*

M O enes, as emerging MXenes-like materials, also have wide structural spaces and various chemical and physical properties. Using first-principles and high-throughput calculations, we have built an online library (<https://moenes.online>) for M O enes family materials from basic summaries, mechanical, phonon and electron aspects, based on their structural diversities from 2 stoichiometric ratios, 11 early-transition metals, 4 typical functional groups and 4 oxygen group elements. Compared to MXenes, the main advantage of M O enes at present is that we have discovered 14 direct semiconductors, which greatly increases the number of direct semiconductors and the range of band gap values in the MXenes family. Among them, 1T-Ti₂OF₂ (O=O, S, Se) reveal tunable semiconducting features and strong light-harvesting ability ranging from the ultraviolet to the near-infrared region. Besides, 2H- and 1T-Y₂TeO₂ have a long carrier lifetime of 2.38 and 1.24 ns, originating from their spatially distinguished VBM and CBM states and long dephasing times. In addition, 2H-Zr₂O(O)₂ shows spin-valley coupling phenomena, and the valley spin splitting is apparent and robust in its conduction band (~ 85 meV). Therefore, M O enes have a wealth of physical properties, not limited to those reported here, and future studies of these emerging M O enes are appealing.

I. INTRODUCTION

The structural space of the two-dimensional (2D) transition metal carbides, nitrides and carbonitrides (MXenes) has a wide range of control possibilities, from abundant early-transition metals, stoichiometric ratios, surface functional groups and solid solution formations[1–3]. Still now, more than 40 types of MXenes with distinct stoichiometry have been successfully synthesized in experiments, and the theoretically predicted number of MXenes is even more unpredictable in view of the formation of its solid solution[3]. In addition, the structural diversity of MXenes gives rise to their variable and tailorable physical and chemical properties. As a result, MXenes have a wide range of applications ranging from energy storage and harvesting to catalysis, water purification and desalination, electromagnetic interference shielding, communications, optics, electronics, plasmonics, sensors, actuators, composites, and biomedicine[4, 5]. However, only Sc₂C(OH)₂[6], Cr₂TiC₂(OH)₂[7] and Y₂C(OH)₂[8] MXenes are direct semiconductors and their band gap values are mainly in the range of 0.71–0.84 eV (HSE06), which severely limits MXenes' applications in the semiconductor field.

Prior to this work, we have extended traditional MXenes to 2D early transition metal-based oxides, M O enes, relying on the regulation of the "X" position in MXenes. Correspondingly, the MXenes-like M O enes have a general formula of M_{n+1}O_nT_x, where M indicates an early-transition metal, where O is the oxygen group element

(O, S, Se and Te), and T_x is the surface functional group, such as hydrogen, hydroxyl, oxygen or fluorine (Fig. 1). In fact, the layer 1T-Ti₂O phases [9, 10], oxycarbide MXenes [11] and Zr₂Se(B_{1-x}Se_x) ($x = 0-0.97$) chalcogenide MAX phases strongly support the experimental feasibility of this emerging M O enes family. Moreover, bare Ti₂O M O enes have promise for electriles, superconductor and anode materials in lithium and sodium batteries [12]. Importantly, Ti₂OX₂ (X = F, Cl) M O enes and their Janus phases are direct semiconductors with a band gap of 0.58–1.18 eV at the hybrid functional (HSE06) level, together with quantum phase transitions, long carrier lifetime, strong light-harvesting ability [13, 14] and superior thermoelectric performance [15, 16]. Terminated 2H-Ti₂O M O enes and their Janus structures also show potentials in piezoelectric transducers and actuators [17]. Besides, 2H-Ti_{n+1}O_n ($n = 1-3$) shows a slightly weakened superconductivity with increasing atomic thickness, 2H-Ti₃O₂F₂/Ti₄O₃F₂ exhibits quantum spin Hall effects at room temperature [18]. Oxidized 2H-M₂O (M= Ti and Zr) M O enes show strong linear and non-linear optical response in the infrared range [19]. Furthermore, when the early-transition metal turns to V, the oxygen-terminated V₂O M O enes are perfect electrocatalysts for the hydrogen evolution reaction [20]. But, not just limited to these, the compositions of M O enes also have highly adjustable space as shown in Fig. 1, and the role of the different "M" and "O" sites in the M O enes is still not clear. Besides, research on M O enes has only just begun, to make the M O enes family we are interested in better known, their fundamental properties, including stability, mechanical properties and electronic structures, are very effective for future research. Therefore, an online library of materials will be a practical way to make getting to know M O enes

* yanluo@usc.edu.cn

† liujiang86@gmail.com

IA		Early transition metal "M"										Possible function group "T"					0							
II		IIA		Oxygen group element "O" $n = 1, 2$										III A					IV A	V A	VIA	VII A	He	
Li	Be											B	C	N	O	F						Ne		
Na	Mg	III B	IV B	V B	VI B	VII B	VIII					IB	II B	Al	Si	P	S	Cl						Ar
K	Ca	Sc	Ti	V	Cr	Mn	Fe	Co	Ni	Cu	Zn	Ga	Ge	As	Se	Br						Kr		
Rb	Sr	Y	Zr	Nb	Mo	Tc	Ru	Rh	Pd	Ag	Cd	In	Sn	Sb	Te	I						Xe		
Cs	Ba		Hf	Ta	W	Re	Os	Ir	Pt	Au	Hg	Tl	Pb	Bi	Po	At						Rn		
Fr	Ra		Rf	Db	Sg	Bh	Hs	Mt	Ds	Rg														

M_{n+1}O_nT₂ (M = early transition metal; O = oxygen group element; T = F, H, O, OH; n = 1, 2)

FIG. 1. The compositions of M_{n+1}O_nT₂ in the periodic table. The green, purple and pink frame represent early transition metal, possible function group (-O, -H, -OH, -F) and oxygen group element (O, S, Se, Te), respectively.

easier. Significantly, M_{n+1}O_nT₂ with direct band gaps are excellent complements to the MXenes. Therefore, the development of the excellent direct semiconductors of M_{n+1}O_nT₂ beyond what we have explored will further expand the application prospects of the MXenes family in the semiconductor field.

In this work, 2H- and 1T-M_{n+1}O_nT₂ (n = 1, 2) M_{n+1}O_nT₂ are fully scrutinized, including 11 early-transition metals, 4 typical functional groups and 4 oxygen group elements (Fig. 1). Using first-principles and high-throughput calculations, the M_{n+1}O_nT₂ are studied and summarized from basic summaries, mechanical properties, phonon spectra and electronic structures. Furthermore, the online materials library for M_{n+1}O_nT₂ has also been built to quickly understand the properties of the desired M_{n+1}O_nT₂. Of the total of 880 M_{n+1}O_nT₂ (n = 1, 2) M_{n+1}O_nT₂ studied here, 464 are dynamically stable and show semimetallic, metallic, semiconducting and (topological) insulating features. The effects of the "M" and "O" sites on the M_{n+1}O_nT₂ have also been studied and compared. In particular, 13 direct semiconductors are newly found beyond Ti₂OX₂ (X = F, Cl) [13] and Ti₂OFCI M_{n+1}O_nT₂ [14], which is a perfect compensation for the defects of MXenes. The direct semiconductors are rare and their bandgap values are concentrated. In this regard, our focus here is on these direct semiconductors with exotic properties, and other aspects merit further research. In particular, 1T-Ti₂SF₂ and 1T-Ti₂SeF₂ have strong infrared and visible light absorption properties by considering electron-hole (e-h) interactions, which can be used in infrared detection and solar energy fields. In addition, the weak nonadiabatic coupling (NAC) induced by spatially distinct valence band maximum (VBM) and the conduction band minimum (CBM) states and the long dephasing time prolong the carrier lifetimes for 2H and 1T-Y₂TeO₂ M_{n+1}O_nT₂, reaching the nanosecond level. Furthermore, the coupled spin and valley physics in 2H-ZrO(O)₂ M_{n+1}O_nT₂ provides another platform to investigate spintronic and valleytronic properties. Unlike MX-

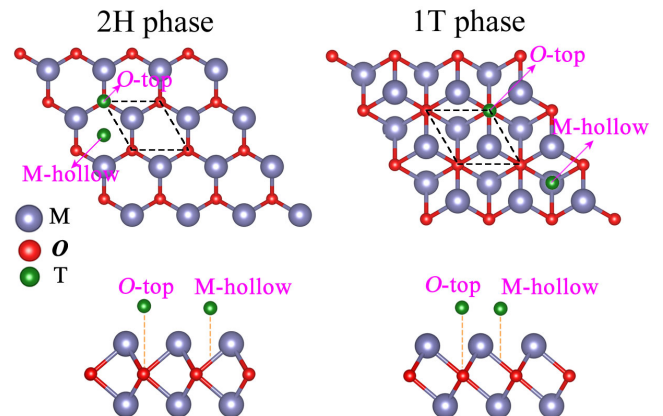


FIG. 2. Top view of (a) 2H- and (b) 1T-M_{n+1}O_nT₂ (n = 1, 2; T = F, H, OH and O) M_{n+1}O_nT₂. Here, the side view of M_{n+1}O_nT₂ is depicted from (c) 2H- and (d) 1T-M₂OT₂. The two possible functionalization sites on either side of the surface are O-top (on the top of the O sites) and M-hollow (on the hollow site of the hexatomic ring of M and O sites). The black line means the primitive cell.

enes, M_{n+1}O_nT₂ exhibit rich semiconducting features and are suitable for future researches in electronics, optoelectronics, photovoltaics, valleytronics, etc.

II. RESULTS AND DISCUSSION

A. Crystal structures of M_{n+1}O_nT₂

The crystal structures of M_{n+1}O_nT₂ M_{n+1}O_nT₂ are shown in Fig. 2. In general, M_{n+1}O_nT₂ have two phases: 2H trigonal prismatic and 1T octahedral phases. As shown in Fig. 2a, the 2H phase consists of edge-sharing trigonal prisms belonging to the space group $P\bar{6}m2$ (No. 184). On the other hand, 1T phase has a space group

System	-bare		-F		-H		-O		-OH	
	2H	1T	2H	1T	2H	1T	2H	1T	2H	1T
Sc ₂ O	/	M	/	M	M	M	/	/	M	M
Y ₂ O	/	M	/	SM	M	M	/	4.67 eV	M	M
Ti ₂ O	M	M	0.20 eV	0.50 eV	M	M	0.18 eV	/	M	M
Zr ₂ O	M	/	0.87 eV	0.88 eV	M	M	0.46 eV	/	M	M
Hf ₂ O	M	/	0.12 eV	0.23 eV	M	M	0.47 eV	/	M	M
V ₂ O	M	M	/	/	M	M	SM	SM	/	/
Nb ₂ O	M	M	M	M	M	M	SM	0.14 eV	M	M
Ta ₂ O	M	M	M	M	M	M	SM	SM	M	M
Cr ₂ O	M		M	M	/	/	/	/	/	/
Mo ₂ O	/	/	/	/	M	/	/	/	M	M
W ₂ O	/	/	/	/	/	/	/	/	/	/

FIG. 3. Summarised information for M_2OT_2 $M\mathcal{O}$ enes, including stability and electronic structural properties distinguished by direct/indirect semiconducting, insulating, metallic and semimetallic features. The red, blue, and purple values represent the band gap values of direct semiconductors, indirect semiconductor, and insulator, respectively.

of $P\bar{3}m1$ (No. 164), and is composed of $[M\mathcal{O}_6]$ octahedra. Due the unsaturated orbitals of outer M metals, bare $M\mathcal{O}$ enes are apt to be terminated by functional groups. In this respect, the most two possible functionalisation sites are considered, as exhibited in Fig. 2. The most energetically stable crystal structures of $M_{n+1}\mathcal{O}_nT_2$ $M\mathcal{O}$ enes can be determined by comparing their energies. In the following, we fully studied the bare $M_{n+1}\mathcal{O}_n$ $M\mathcal{O}$ enes and terminated $M_{n+1}\mathcal{O}_nT_2$ $M\mathcal{O}$ enes from dynamical, mechanical and electronic features by high-throughput calculations.

B. Online materials library for $M\mathcal{O}$ enes

To give a quick understanding for this emerging $M\mathcal{O}$ enes family, we firstly have built an online materials library (<http://moenes.online>). The workflow for investigating $M\mathcal{O}$ enes is shown in Fig. S1. Based on the most energetically stable $M_{n+1}\mathcal{O}_n$ and $M_{n+1}\mathcal{O}_nT_2$ $M\mathcal{O}$ enes, we firstly confirm the ground states of $M\mathcal{O}$ enes by comparing energies between nonmagnetic (NM) and ferromagnetic (FM) spin configurations. Phonon spectra of $M\mathcal{O}$ enes are next used to confirm their dynamical stability. Besides, their mechanical stability are determined by Born criteria for hexagonal crystal, namely, $C_{11} > |C_{12}|$ and $C_{66} = (C_{11} - C_{12})/2 > 0$ [21]. When $M\mathcal{O}$ enes have reliable dynamical and mechanical stability, the electronic properties of $M\mathcal{O}$ enes are explored, and then their band characters can be determined by the locations of the VBM and CBM).

In brief, the structures of 880 $M\mathcal{O}$ enes have been presented in this online materials library, from basic summaries to mechanical properties, phonon spectra and

band structures. One can quickly search for the characteristics of the desired $M\mathcal{O}$ enes by selecting stoichiometric ratios (n), early-transition metals (M), oxygen group elements (\mathcal{O}) and functional groups (T) step by step. Taking Ti_2SF_2 $M\mathcal{O}$ enes as illustrations, the search results are shown in Fig. S2. In basic summaries part, we can obtain the optimized lattice constant, favorable absorption site, the most favourable dynamical stability, magnetic moments of early-transition metal, locations of VBM and CBM, band character, band gap in semiconductors/insulators and work functions, etc. In mechanical properties part, the elastic constants, mechanical stability, Young's modulus (Y) and poisson's ratio (ν) are available. In addition, we can acquire their phonon dispersions within the phonon spectra, and projected band structures (Pbands) are provided as well.

The stability, exotic electronic features including semimetals, direct/indirect semiconductors and insulators are also summarized. The summaries for M_2OT_2 $M\mathcal{O}$ enes are shown in Fig. 3. There are 70 M_2OT_2 $M\mathcal{O}$ enes are dynamically stable. Obviously, most of them have rich metallic properties, along with several semimetals, such as 1T- Y_2OF_2 , 2H- $M_2O(O)_2$ ($M=V, Nb, Ta$) and 1T- $M_2O(O)_2$ ($M=V, Ta$), in which the Weyl fermion locates at the Fermi level. Besides, there are 10 semiconductors and one insulators. Among them, 2H/1T- Ti_2OF_2 , 2H- $M_2O(O)_2$ ($M = Zr, Hf$) and 1T- $Nb_2O(O)_2$ are direct semiconductor with a band gap of 0.14–0.50 eV(PBE). 2H/1T- M_2OF_2 ($M = Zr, Hf$) and 2H- $Ti_2O(O)_2$ are indirect semiconductors. Besides, 1T- $Y_2O(O)_2$ is an insulator with a band gap of 4.67 eV (PBE), and futher corrected to 6.20 eV (HSE06). It is worth emphasizing that the summaries for M_2ST_2 , M_2SeT_2 , M_2TeT_2 , $M_3O_2T_2$, $M_3S_2T_2$, $M_3Se_2T_2$ and

$M_3Te_2T_2$ MOenes are available in Supporting Informations. As listed in Table 1 and shown in Fig. S11, there are 14 direct semiconductors in the MOenes family, and their band gap values are 0.32–1.28 eV (HSE06), reflecting their promising applications in semiconducting fields. Furthermore, they have a small Y (< 260 N/m) and isotropic ν , meaning their soft properties, and thus can be applied in flexible devices [22].

TABLE I. The bandgaps of direct semiconductors, evaluated by PBE (E_g in eV) and HSE06 (E_g^{hse} in eV), along with their Y (N/m) and ν .

Systems	E_g	E_g^{hse}	Y	ν
2H-Ti ₂ OF ₂	0.20	0.82	230.80	0.19
1T-Ti ₂ OF ₂	0.50	1.18	229.90	0.18
2H-Zr ₂ O(O) ₂	0.46	1.28	149.80	0.21
2H-Hf ₂ O(O) ₂	0.47	1.24	139.79	0.26
1T-Nb ₂ O(O) ₂	0.14	0.90	251.96	0.37
1T-Ti ₂ SF ₂	0.15	0.67	170.60	0.17
1T-Zr ₂ SF ₂	0.35	0.78	168.94	0.19
2H-Hf ₂ SF ₂	0.11	0.38	179.32	0.25
1T-Ti ₂ SeF ₂	0.33	0.97	164.48	0.15
2H-Zr ₂ SeF ₂	0.17	0.42	141.74	0.24
1T-Zr ₂ SeF ₂	0.70	1.23	166.88	0.16
2H-Y ₂ TeO ₂	0.84	1.27	137.40	0.37
1T-Y ₂ TeO ₂	0.79	1.18	142.28	0.36
2H-Hf ₃ Se ₂ F ₂	0.15	0.32	233.57	0.22

As presented above, the bare MOenes are metals and usually lack a good stability, but they can transform into dynamically stable phases when their outer orbitals of M are saturated by functional groups. On the other hand, the electronic traits of MOenes are strongly related to the M. In short, the majority of fluorinated and hydroxidized Ti-, Zr-, Hf-based MOenes show semiconducting features, and other fluorinated and hydroxidized MOenes are mostly metallic. In addition, oxidized Sc- and Y-based M₂O MOenes have insulating and semiconducting characters, but oxidized V-, Nb-, Ta-based M₂O MOenes possess semimetal and metallic features. All in all, due to the structural diversity of MOenes, it brings the diversity of its electronic structures, including highly conductive metallic, semimetallic, semiconducting, (topological) insulating, which can bring various applications for MOenes as traditional MXenes.

C. The effect of "M" site on MOenes

Since early transition metal elements bring rich electronic structures in MOenes, we have selected group IVB metal elements (Ti, Zr, Hf) and fifth-row transition metal elements (Y, Zr, Nb, Mo) under the chemical formula 1T-M₂OF₂ to fully characterize the influence of "M" sites in MOenes (Fig. 4a). In all fluorinated 1T-M₂O MOenes, because of the lower electronegativity of the transition metals than the O atom and the attached flu-

orinated functional groups, the transition metals become positively charged by donating their electrons to both O atoms and the fluorinated functional groups. Firstly, Ti, Zr, and Hf are in the same IVB group in the periodic table with the same number of electrons in their outer shells ([Ar]3d²4s², [Kr]4d²5s², and [Xe]4f¹⁴5d²6s²). As expected, fluorinated 1T-Zr₂O and Hf₂O exhibit similar semiconducting properties to those of 1T-Ti₂OF₂ [13]. Moreover, their energy states around the Fermi energy are mainly made of the M- d_{z^2} and M- $d_{x^2-y^2}$ (M = Ti, Zr and Hf) orbitals. As shown in Fig. 4b, 1T-Ti₂OF₂ is a direct semiconductor together with VBM and CBM located at the Γ point. However, when M changes from Ti, to Zr, and even to Hf, the M- d_{z^2} orbitals move down, while the M- $d_{x^2-y^2}$ orbitals move up. As a result, the M- $d_{x^2-y^2}$ at the K point is higher than the M- d_{z^2} at the Γ point in. Thus, 1T-Zr₂OF₂ and 1T-Hf₂OF₂ become indirect semiconductors (Fig. 4c and 4d).

Around the Zr metal element, the fifth-row transition metal elements (Y, Zr, Nb) are further systematically scrutinized to draw the roles of the different number of electrons in their outer shells ([Kr]4d¹5s², [Kr]4d²5s², [Kr]4d⁴5s²). Due to the dynamical instability in 1T-Mo₂OF₂, we don't consider it further. Clearly shown in Pbands, as the number of electrons in Y, Zr and Nb outer shells progressively increases, the Fermi energy gradually shifts upwards and the $d_{x^2-y^2}$ orbitals near the Fermi energy move down largely. As Zr changes to Nb metal, the increase of Fermi energy and the movement of Nb- $d_{x^2-y^2}$ orbitals result in the metal characters for 1T-Nb₂OF₂ (Fig. 4f). When the Zr turns to Y, the Fermi energy shifts downwards and cuts directly through the middle of the most highest valance bands in 1T-Zr₂OF₂, leading to a semimetal feature for 1T-Y₂OF₂ (Fig. 4e). Clearly, two salient features can be observed in 1T-Y₂OF₂ without SOC (Figs. 4e and S12a). Firstly, 1T-Y₂OF₂ has two linear band crossings in the Fermi level (P₁ and P₂). Secondly, these linear band crossings are observed for an electron and hole band near the Fermi level. A careful scan of the band structure shows that the intersection P₁ is not isolated, but is actually part of an approximate nodal loop centred on the Γ point, as indicated in Figs. S12c and S12e. However, the approximate nodal ring is not complete, and the exact crossing points are located only on the high symmetry path, such as P₁. Remarkably, the crossing points (labeled N₁ and N₂) still persist when SOC is turned on (Fig. S12b), which is similar to that without SOC due to the weak SOC effect in 1T-Y₂OF₂. The difference is that each band, when considering SOC, is doubly degenerate. Moreover, a complete nodal ring (labeled L₁) exists around the Γ point at this time, as shown by the calculated energy gap between the electron-like and hole-like bands in Fig. S12f. Since each band is doubly degenerate, the nodal ring is fourfold degenerate Dirac nodal ring, as illustrated in Fig. S12d. In addition, the Dirac nodal ring of this system lies exactly on the Fermi surface and there are no non-topological bands near the Fermi energy, reflecting the properties of

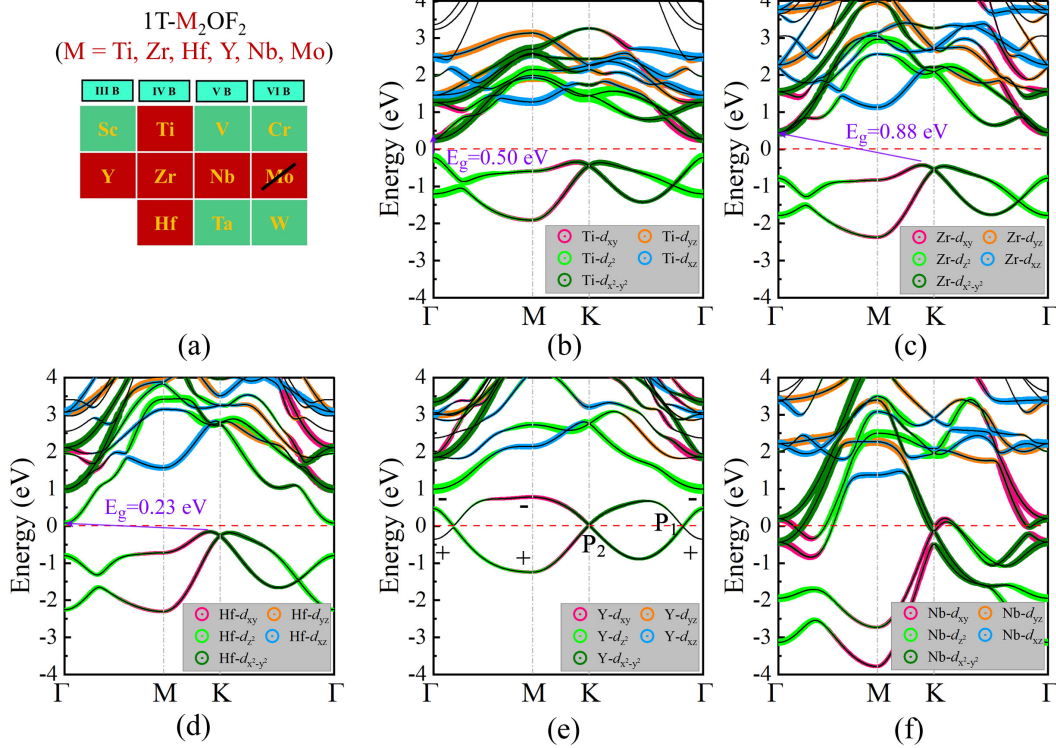


FIG. 4. (a) Selected early transition metals in the periodic table. Bands at PBE level for (b) 1T-Ti₂O₂F₂, (c) 1T-Zr₂O₂F₂, (d) 1T-Hf₂O₂F₂, (e) 1T-Y₂O₂F₂ and (f) 1T-Nb₂O₂F₂, weighted by their *d* orbitals. Signs "+" and "-" in (e) represents the symmetries of parity. The Fermi level is set to 0 eV.

an ideal 2D Dirac nodal loop state.

D. The effect of "O" site on MOenes

In order to draw the influence of oxygen group elements, the properties of Ti₂O₂F₂ (O = O, S, Se, Te) are systematically scrutinized and compared. We first focused on the 1T phase. Firstly, 1T-Ti₂SF₂, 1T-Ti₂SeF₂ and 1T-Ti₂TeF₂ can maintain structural integrity at 900, 600 and 300 K, respectively (Fig. S13), lower than that of 1T-Ti₂O₂F₂ (1200 K)[13]. Clearly, as the oxygen group elements change from O to S, Se and Te, the thermal stability is weakened due to the increase in chemical bonds. (Table II). Similar to 1T-Ti₂O₂F₂ shown in Fig. 5a [13], 1T-Ti₂SF₂ and 1T-Ti₂SeF₂ are direct semiconductors with VBM and CBM located at the Γ point, and have a band gap of 0.67 and 0.97 eV (HSE06), respectively (Figs. 5c and 5e). The sum of square of the transition dipole moment (P^2) also confirm the allowed electronic transition between VBM and CBM at the Γ point. Their VBM states are composed of Ti-*d*_{z²} orbitals mostly, but CBM states have hybrid orbitals from Ti-*d*_{xy}, Ti-*d*_{z²} and Ti-*d*_{x²-y²}. The same as 1T-Ti₂O₂F₂ monolayer [13], three low-energy bands are involved in the band edges at Γ point, including one valence band and two degenerate conduction bands composed by one heavy electron-band

and one light electron-band. Besides, 1T-Ti₂TeF₂ monolayer has an indirect band gap of 0.40 eV (HSE06), which is also reflected by the results of P^2 (Fig. 5g). As expected, their band gaps at the Γ point first decrease and then increase when the oxygen group elements change from O to S, Se and then to Te. This is due to the decrease in electronegativity of the oxygen group elements, which weakens the bond strength in the 1T-Ti₂O₂F₂ (O = O, S, Se, Te) MOenes (Table II). The clearer Pbands are shown in Fig. S14. As the oxygen group elements change from O to S, the light electron-band contributed by Ti-*d*_{z²} orbitals moves down and gradually becomes a heavy electron-band, leading to a decrease of the band gap firstly. When the oxygen group elements change from S to Se, this band continuously moves down and the orders of the original two degenerate conduction bands are changed, bringing an increase of the band gap. In this progress, the band dispersions of two degenerate conduction bands and valence band around the Γ point have been significantly weighted, leading to a larger effective mass and a smaller carrier mobility. Finally, 1T-Ti₂TeF₂ monolayer becomes an indirect semiconductor with VBM and CBM located at the Γ and M point, respectively.

As the oxygen group elements change progressively, the optical absorption behaviour of 1T-Ti₂O₂F₂ (O = O, S, Se, Te) are further compared within a GW method simulated with the random phase approximation (GW+RPA)

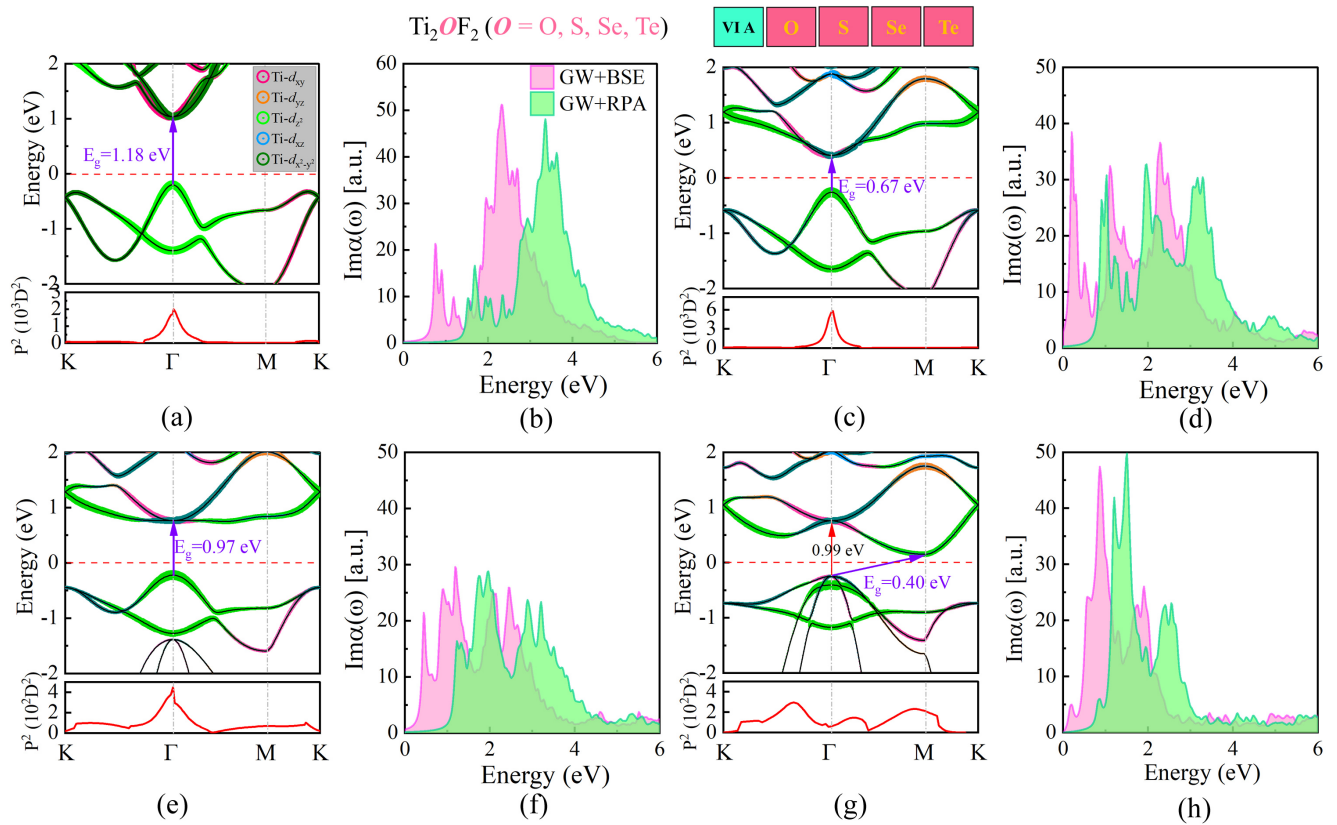


FIG. 5. Pbands (upper plane) along with P^2 (lower plane) for (a) 1T-Ti₂OF₂, (c) 1T-Ti₂SF₂, (e) 1T-Ti₂SeF₂ and (g) 1T-Ti₂TeF₂, calculated at the HSE06 level. Imaginary part of the macroscopic polarizability of (b) 1T-Ti₂OF₂, (d) 1T-Ti₂SF₂, (f) 1T-Ti₂SeF₂ and (h) 1T-Ti₂TeF₂ calculated on the basis of GW+RPA and GW+BSE methods.

(without e-h interactions) and the Bethe-Salpeter equation (GW+BSE) (with e-h interactions). The imaginary parts of the frequency-dependent 2D polarizability for 1T-Ti₂SF₂, 1T-Ti₂SeF₂ and 1T-Ti₂TeF₂ are shown in Figs. 5d, 5f and 5h, respectively, and compared with that for 1T-Ti₂OF₂ (Fig. 5a)[13]. Here, the optical band gap E_g^o is defined as the first dominated peak corresponding to the first optically allowed (bright) exciton. The E_g^o values for 1T-Ti₂SF₂, 1T-Ti₂SeF₂ and 1T-Ti₂TeF₂ are 0.21 and 0.45 eV, respectively. In term of the spectral edge obtained at the GW+RPA level, the quasi-particle energy gap (G_0W_0 gap) are extracted to 0.74 (1.05) eV for 1T-Ti₂S(Se)F₂. Here, GW correction to the PBE band gap is about 0.59 (0.70) eV. Then, the exciton binding energy E_b values for 1T-Ti₂SF₂ and 1T-Ti₂SeF₂ are evaluated to 0.53 and 0.59 eV, respectively. As listed in Table II, the numerical values of the E_g^o and G_0W_0 gap show the same trend as the band gap values. Generally, the larger the band gap, the weaker the screening, resulting in a higher E_b . Therefore, the E_b values of 1T-Ti₂OF₂ ($\text{O} = \text{O}, \text{S}, \text{Se}$) decrease firstly, and then increase, on going from O to Se. Similar to 1-Ti₂OF₂ monolayer[13], there are several significant peaks in the infrared and visible light regions, making 1T-Ti₂OF₂ ($\text{O}=\text{S}, \text{Se}, \text{Te}$) promising for infrared detectors and solar cells with strong light

absorption ability in the desired spectral range.

On the other hand, as the oxygen group elements gradually change from O to Te, the 2H-Ti₂OF₂ ($\text{O} = \text{O}, \text{S}, \text{Se}, \text{Te}$) changes from a direct semiconductor to a Weyl semimetal, and finally to an indirect semiconductor (Fig. S15) at the PBE level, undergoing a similar evolution of the Ti- d_{z^2} orbitals discussed above. When spin-orbit coupling (SOC) is not considered, the Weyl fermions in 2H-Ti₂SF₂ and 2H-Ti₂SeF₂ are purely located at the Γ point at the Fermi level (Figs. S16a and 16d). At this time, the VBM and CBM touch quadratically and form a two-component 2D double Weyl fermion with an E' irreducible representation of the D_{3h} point group. When SOC is considered, these degenerate Weyl fermions contributed by Ti- d_{xy} and Ti- $d_{x^2-y^2}$ orbitals are split, resulting in a SOC gap of ~ 19 and 9 meV (PBE) for 2H-Ti₂SF₂ and 2H-Ti₂SeF₂, respectively (Figs. S16b and S16e). Moreover, in Figs. S16c and 16f, the edge states depicted 2H-Ti₂SF₂ and 2H-Ti₂SeF₂ connect the bulk valence and conduction bands. Besides, the Z_2 invariant values are determined to be 1 via Wannier charge center calculations. Thus, 2H-Ti₂SF₂ and 2H-Ti₂SeF₂ are determined to be 2D topological insulators, whose non-trivial gaps are further corrected to ~ 24 and 55 meV (HSE06). Although these nontrivial gaps are smaller

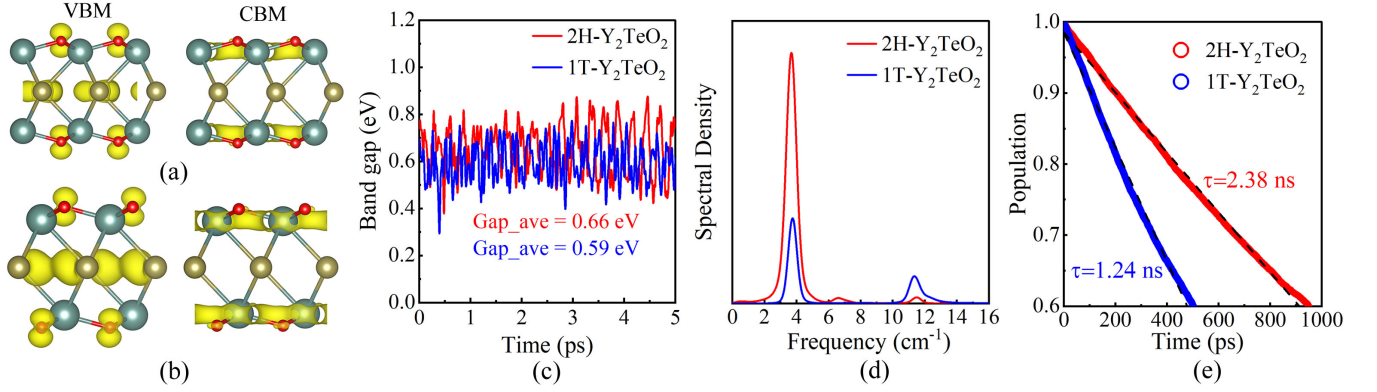


FIG. 6. Band decomposed charge density of VBM and CBM at the Γ point for (a) 2H- and (b) 1T-Y₂TeO₂. (c) The variations of band gaps during the 5ps' AIMD simulations. (d) Spectral densities and (e) excited-electron population decay.

than that in Ti₃O₂F₂ and Ti₄O₃F₂ MOenes, they are adequate for practical applications at room temperature [18].

TABLE II. Optical band gaps E_g^o (eV), G_0W_0 gap (eV), exciton binding energy E_b (eV), and chemical bond length (\AA) for 1T-Ti₂OF₂ ($O = O, S, Se, Te$) MOenes.

Systems	E_g^o	G_0W_0 gap	E_b	Ti-O	Ti-F
1T-Ti ₂ OF ₂	0.76	1.37	0.61	2.15	2.09
1T-Ti ₂ SF ₂	0.21	0.74	0.53	2.47	2.15
1T-Ti ₂ SeF ₂	0.45	1.05	0.59	2.60	2.17
1T-Ti ₂ TeF ₂	0.19	0.64	0.45	2.79	2.19

E. Exotic direct semiconductors in MOenes

As summarized before, the most significant advantage identified thus far is that MOenes markedly enhance the scope of direct semiconductors and light absorption within the MXenes family. Therefore, we put our attention on these direct semiconducting MOenes with fascinating properties in the following.

1. Long carrier lifetime in 2H- and 1T-Y₂TeO₂ MOenes

Carrier lifetime is critical in optoelectronic devices, where nonradiative (NA) electron-hole (e-h) recombination is the dominant factor. In term of Fermi's golden rule [23], the NA e-h recombination rate is the e-h recombination rate is proportional to the square of the NAC constant, which is defined as [24]:

$$d_{ij} = \langle \varphi_j | \frac{\partial}{\partial t} | \varphi_k \rangle = \sum_I \frac{\langle \varphi_j | \nabla_{R_I} \mathcal{H} | \varphi_k \rangle}{\varepsilon_k - \varepsilon_j} \dot{\mathbf{R}}_I, \quad (1)$$

where \mathcal{H} is the Kohn-Sham Hamiltonian, $\varphi_{j/k}$ and $\varepsilon_{j/k}$ indicates the wave functions and eigenvalues for

electronic states j/k , respectively. Here, the states j and k are CBM and VBM, respectively. Obviously, smaller electron-phonon (e-ph) coupling elements ($\langle \varphi_j | \nabla_{R_I} \mathcal{H} | \varphi_k \rangle$) determined by the wave function overlap between VBM and CBM and the e-ph interactions, smaller nuclear velocity $\dot{\mathbf{R}}_I$ that is roughly proportional to atomic mass [25], and larger energy gap ($\varepsilon_k - \varepsilon_j$) will lead to weaker NAC.

Interestingly, the VB and CB band edge states of 2H- and 1T-Y₂TeO₂ MOenes are occupied by different component (Figs. S11m and S11l), and as spatial charge density shown in Fig. 6a and 6b, the VBM states are mostly from Te atoms and O atoms, but the CBM states are fully contributed by Y atoms. Therefore, the spatially distinguished VBM and CBM states indicate a long carrier lifetime [13, 26–28]. Firstly, 2H- and 1T-Y₂TeO₂ not only possess dynamical and mechanical stability, but also have a good stability at 300 K (Figs. S16a and S15b). Next, the NAC values for 2H- and 1T-Y₂TeO₂ are obtained to be 0.95 and 1.18 meV, respectively, which are greatly smaller than that in 2H-Ti₂OF₂ (2.46 meV) and 1T-Ti₂OF₂ (3.10 meV) [13]. The fluctuations of band gap values (PBE) at 300 K are exhibited in Fig. 6c, and the averaged band gaps for 2H- and 1T-Y₂TeO₂ are 0.66 and 0.59 eV, respectively. Compared to the band gaps at 0 K (Table I), the band gaps decrease about 0.2 eV, due to the thermal distortions [29]. In order to understand the phonon modes engaged in the e-h recombination and the relative e-ph interactions in Y₂TeO₂, the Fourier transforms of autocorrelation functions of the energy gap fluctuation along MD trajectory, known as spectral densities or influence spectra, is plotted in Fig. 6d. Clearly, a dominate peak appears at around 3.8 THz and a negligible peak locates at 11.7 THz, reflecting the low frequency regions contribute major rules in e-ph interactions. The vibrational modes around 3.8 THz at the Γ point for 2H- and 1T-Y₂TeO₂ are visualized at Figs. S18a and S18b, respectively, where out-of-plane Y and O atom vibrations are participated in the e-h recombination. Moreover, although the e-ph interaction for 2H-Ti₂OF₂ is stronger

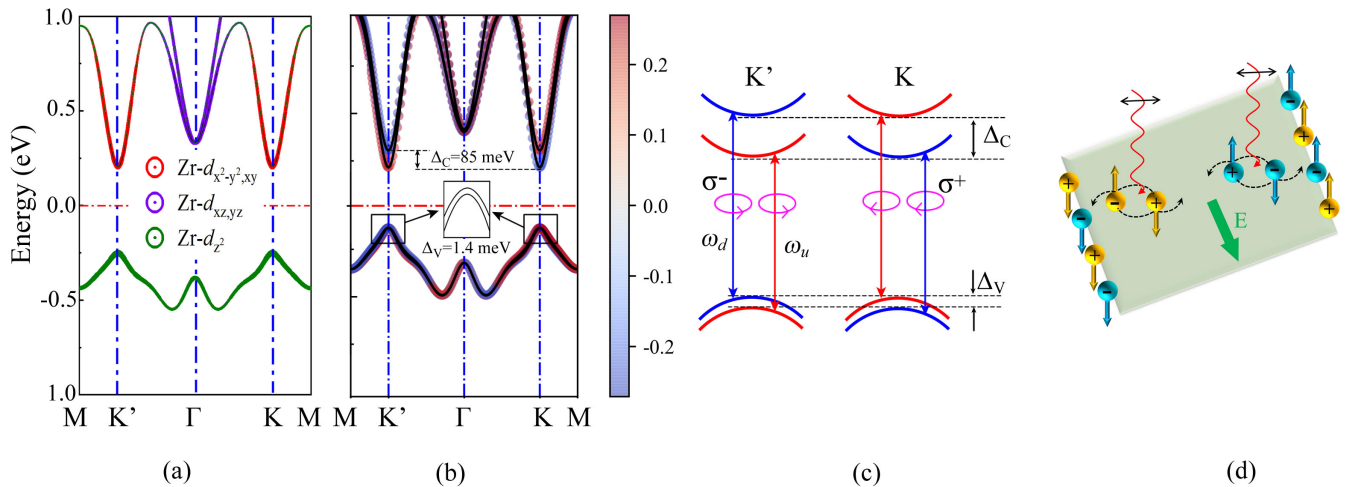


FIG. 7. (a) Pbands and (c) spin projected band structure for $2H-Zr_2O(O)_2$. The blue color in (b) indicate the spin-down states, while red color denotes spin-up states (spin orientation is along out-of-plane direction). The Fermi level is set to 0 eV. (c) VSS in the VBM and the CBM at K/K' valleys, together with scheme of valley-dependent optical selection rules. Here, σ^+/σ^- represents the right/left-hand polarized light, which couples to the band edge transition at the K/K' valley. (d) Spin and valley Hall effects under linearly polarized optical field with a frequency ω_u . Yellow and cyan balls indicate carriers in K' and K valleys, respectively, and the +/- symbol in the ball represents a hole/electron.

than that of $1T-Ti_2OF_2$, $1T-Ti_2OF_2$ has a larger band gap, resulting in a weaker NAC. All in all, the small NAC in Y_2TeO_2 MOenes will greatly prolong the carrier lifetime.

By using Hefei-NAMD code [24], the carrier lifetimes of 2H- and $1T-Y_2TeO_2$ are obtained. Generally, e-ph interactions are from inelastic and elastic scattering, where inelastic scattering transfers extra energy to involved nuclei, resulting in a NA recombination process; elastic scattering destroys the coherence in a quantum-mechanical superposition between VBM and CBM, leading to decoherence (also named as pure-dephasing) [29]. Therefore, the decoherence has been considered into NAMD algorithm, and the decoherence time can be obtained by fitting the pure-dephasing functions with a Gaussian, $\exp[-0.5(t/T)^2]$, plotted in Fig. S18c. The pure-dephasing time for 2H- and $1T-Y_2TeO_2$ are calculated to 6.58 and 8.59 fs, respectively, which are smaller than that for $2H-Ti_2OF_2$ (20.11 fs) and $1T-Ti_2OF_2$ (11.26 fs) [13]. When $2H-Y_2TeO_2$ is compared to $1T-Y_2TeO_2$, the transition energy with larger fluctuations (Fig. 7c) leads to a faster pure dephasing time, *i.e.* a longer e-h recombination. Furthermore, the evolution of an excited electron state population is plotted to evaluate the carrier lifetime, as described in Fig. 6e. By fitting of a short-time linear expansion to the exponential decay, $f(t)=\exp(-t/\tau) \approx 1-t/\tau$, the carrier lifetime for 2H- and $1T-Y_2TeO_2$ are calculated to be 2.38 and 1.24 ns, respectively. Due to the weaker NAC and longer pure-dephasing time, their carrier lifetimes are much longer than that of $2H-Ti_2OF_2$ (0.03 ns) and $1T-Ti_2OF_2$ (0.37 ns) at the PBE level. Specially, the carrier lifetimes for 2H- and $1T-Y_2TeO_2$ can reach the nanosecond scale, comparable to some 2D ma-

terials, such as pristine and doped BP (0.39–5.34 ns) [25], MoS_2 (0.16 ns), $MoSe_2$ (0.21 ns), $MoSSe$ (0.24 ns) [28], and $MoSTe$ (1.31 ns) [30]. Therefore, long excited carrier lifetimes in Y_2TeO_2 MOenes can facilitate the dissociation of excitons into free electron and hole carriers, favouring their fascinating performance in optoelectronic filed.

2. Conduction-band valley spin splitting in $2H-Zr_2O(O)_2$ MOenes

$2H-Zr_2O(O)_2$ and $2H-Hf_2O(O)_2$ MOenes are direct semiconductors together with the band energy extrema at the high symmetry K point (Fig. S11c and 11d). The same symmetry as group IV and VI transition metal dichalcogenide monolayers (TMDs) [31–33], the simultaneous existence of a direct band gap at the K point and a decoupled band edge would provide a platform for exploring valleytronic and spintronic features. However, $2H-Hf_2O(O)_2$ are thermally unstable at room temperature (Fig. S17d). Therefore, in the following we will only concentrate on the $2H-Zr_2O(O)_2$ MOenes with a thermal stability (Fig. S17c).

We then study the electronic band structures of $2H-Zr_2O(O)_2$. Note that the exact gap value has little influence on the main features of the valley characters, so we will base our discussion mainly on the PBE band structures [34–36]. Pbands in the absence of SOC is shown in Fig. 7a. Apparently, $2H-Zr_2O(O)_2$ has a direct band gap of 0.46 eV, together with VBM and CBM located at the same high symmetry K/K' point, which are the two inequivalent corners of the hexagonal Brillouin zone.

Moreover, $2\text{H-Zr}_2\text{O}(\text{O})_2$ has two valleys at the K and K', which are related to each other by time reversal symmetry. When the relativistic effect is included, the spin projected band structure in Fig. 7b shows that the spin-up and spin-down states near CBM have a splitting of ~ 85 meV (Δ_C), whereas the valley spin splitting (VSS) near VBM (Δ_V) is very small (~ 1.4 meV). In contrast to group IV and VI TMDs, where the large VSS is generated at VBM. As we known, the large VSS observed at CBM for $2\text{H-Zr}_2\text{O}(\text{O})_2$ is extremely rare, reported only in $2\text{H-Tl}_2\text{O}$ (~ 610 meV) [37] and 2H-HfN_2 (~ 314 meV) [38]. In subsequent, the orbital contributions give a deeper insight into the different behaviour of VSS at CBM and VBM. The CBM is predominantly contributed by Zr- $d_{x^2-y^2,xy}$, and the dominant orbital occupations for VBM are Zr- d_{z^2} . Thus, given that the C_s symmetry guarantees the out-of-plane potential gradient symmetry, the VSS in $2\text{H-Zr}_2\text{O}(\text{O})_2$ arises mainly from the in-plane potential gradient asymmetries. Due to its out-of-plane orientation, Zr- d_{z^2} has no effect on the VSS at VBM. On the other hand, the in-plane characters of Zr- $d_{x^2-y^2,xy}$ states contribute the VSS at CB. Subsequently, the weak SOC strength within the Zr atom results in the tiny splitting for $2\text{H-Zr}_2\text{O}(\text{O})_2$, comparable to that of MoSSe ($\Delta_{C/V} = 13.7/170$ meV) [39] and MoSe₂ ($\Delta_V = 180$ meV) [40]. In addition, by choosing a suitable substrate [38], larger VSS can be expected in $2\text{H-Zr}_2\text{O}(\text{O})_2$. Similar to $2\text{H-Tl}_2\text{O}$ [37], the magnitudes of the VSS in both CBM (Δ_C) and VBM (Δ_V) are robust against mechanical deformation (Fig. S19), favoring its realistic applications.

For two inequivalent K and K' valleys, time-reversal symmetry generally leads to the opposite ordering of spin-up and spin-down states. In this regard, spin can be selectively excited through the optical selection rule. Furthermore, by using various circular polarizations and frequencies of optical illumination, the carriers can be selectively stimulate with different combinations of spin and valley indexes [37, 41]. As described in Fig. 7c, the interband transitions at K valley only relates to right-handed circularly polarized light (σ^+), and left-handed circularly polarized light (σ^-) excites the carriers at K' valley. Therefore, under the excitations with left-hand polarized light with a frequency ω_u , spin-up electrons and spin-down holes can be populated in the K' valley. As for K valley, spin-down electrons and spin-up holes can be generated when applying right-band polarized light with a frequency ω_u . Furthermore, the linearly polarized light is the combination of right-handed and left-banded circularly polarized light, and thus can excite the electrons and holes in both K and K' valley. As illustrated in Fig. 7d, when the linearly polarized light is under a frequency ω_u , spin-up electrons and spin-down holes are regulated to K' valley, while spin-down electrons and spin-up holes

can be generated in K valley. In addition, due to the opposite Berry curvatures in CBM and VBM, the excited electrons and holes in the same valley will acquire opposite transverse velocities under an in-plane electric field [37]. This leads to spin-up electrons (holes) from valley K' (K) are accumulated at one boundary, and the spin-down holes (electrons) from valley K' (K) are accumulated at the opposite boundary. In this process, the spin and valley Hall currents occur and bring the coexistence of spin and valley Hall effects. Since both electrons and holes are accumulated at boundary, the charge neutrality will be maintained, thus, the charge Hall current will not be observed. In this case, each boundary will carry a net spin and a valley polarization. Moreover, at a given boundary, the e-h recombinations are not allowed, because both flip spin and valley indices are required, giving a protected valley-spin coupling.

III. CONCLUSIONS

In conclusion, we have systematically investigated the $\text{M}_{n+1}\text{O}_n\text{T}_2$ MOenes family, and have built an online material library. In addition, the roles of "M" and "O" sites are investigated, and $1\text{T-Ti}_2\text{OF}_2$ exhibits an ideal two-dimensional Dirac nodal loop state. What's more surprising is that there are 14 direct semiconductors among the $\text{M}_{n+1}\text{O}_n\text{T}_2$ MOenes, greatly expanding the direct semiconductors in the MXenes family and extending their light absorption range. In particular, we focus on several direct semiconductors with unique features in MOenes family. $1\text{T-Ti}_2\text{OF}_2$ (O=O, S, Se) have a direct band gap of $0.67-1.18$ eV (HSE06), and show strong light absorption ability from the infrared to the ultraviolet region. Besides, inspired by the spatially distinguished VBM and CBM states in 2H- and 1T- Y_2TeO_2 , they possess a long carrier lifetime of 2.38 and 1.24 ns, respectively. In addition, conduction-band VSS is found in $2\text{H-Zr}_2\text{O}(\text{O})_2$, providing an alternate candidate for manipulating the coupled spin and valley physics. Of course, the properties of emerging MOenes are not limited to these and deserve to be explored in the future.

ACKNOWLEDGEMENTS

This work is supported by the Natural Science Foundation of China (Grant No. 12374057), the Startup funds of Outstanding Talents of UESTC (A1098531023601205), National Youth Talents Plan of China (G05QNQR049). B.-T.W. acknowledge financial support from the Natural Science Foundation of China (Grants No. 11675195 and No. 12074381) and Guangdong Basic and Applied Basic Research Foundation (Grant No. 2021A1515110587).

[1] M. Naguib, M. Kurtoglu, V. Presser, J. Lu, J. Niu, M. Heon, L. Hultman, Y. Gogotsi, and M. W. Barsoum,

- [2] J. Halim, S. Kota, M. R. Lukatskaya, M. Naguib, M.-Q. Zhao, E. J. Moon, J. Pitock, J. Nanda, S. J. May, Y. Gogotsi, *et al.*, *Adv. Func. Mater.* **26**, 3118 (2016).
- [3] M. Naguib, M. W. Barsoum, and Y. Gogotsi, *Adv. Mater.* **33**, 2103393 (2021).
- [4] X. Jiang, A. V. Kuklin, A. Baev, Y. Ge, H. Ågren, H. Zhang, and P. N. Prasad, *Phys. Rep.* **848**, 1 (2020).
- [5] A. VahidMohammadi, J. Rosen, and Y. Gogotsi, *Science* **372**, eabf1581 (2021).
- [6] Y. Lee, Y. Hwang, and Y.-C. Chung, *ACS Appl. Mater. & Inter.* **7**, 7163 (2015).
- [7] J. Yang, X. Zhou, X. Luo, S. Zhang, and L. Chen, *Appl. Phys. Lett.* **109**, 203109 (2016).
- [8] D. Wang, H. Li, L. Zhang, Z. Sun, D. Han, L. Niu, X. Zhong, X. Qu, and L. Yang, *Appl. Surf. Sci.* **478**, 459 (2019).
- [9] Y. Fan, C. Zhang, X. Liu, Y. Lin, G. Gao, C. Ma, Y. Yin, and X. Li, *J. Alloys Compd.* **786**, 607 (2019).
- [10] R. Wang, K. Wang, H. Tao, W. Zhao, M. Jiang, J. Yan, and K. Jiang, *J. Mater. Chem. A* **8**, 11224 (2020).
- [11] P. P. Michałowski, M. Anayee, T. S. Mathis, S. Kozdra, A. Wójcik, K. Hantanasirisakul, I. Józwiak, A. Piątkowska, M. Moździońek, A. Malinowska, *et al.*, *Nat. Nanotechnol.* **17**, 1192 (2022).
- [12] L. Yan, T. Bo, B.-T. Wang, S. Tretiak, and L. Zhou, *J. Phys. Chem. Lett.* **12**, 494 (2020).
- [13] L. Yan, J. Zhu, B.-T. Wang, J. He, H.-Z. Song, W. Chu, S. Tretiak, and L. Zhou, *Nano Lett.* **22**, 5592 (2022).
- [14] L. Yan, J. Zhu, Q. Li, R. Ku, X. Huang, B.-T. Wang, H.-Z. Song, S. A. Yang, and L. Zhou, *Appl. Phys. Lett.* **122**, 043101 (2023).
- [15] Y.-L. Wan, Q. Yang, T. Zhang, Z.-Y. Zeng, and X.-R. Chen, *J. Appl. Phys.* **135** (2024).
- [16] Y.-L. Wan, C.-E. Hu, H.-Y. Geng, and X.-R. Chen, *Appl. Surf. Sci.* , 161766 (2024).
- [17] J. Qiu and J. Liu, *Mater. Lett.* , 136620 (2024).
- [18] L. Yan, Y. Huo, J. Zhu, A. Huang, R. Ku, B.-T. Wang, T. Li, and L. Zhou, *Phys. Rev. B* **110**, 045421 (2024).
- [19] A. Huang, L. Ji, Q. Li, Y. Wu, Y.-m. Ding, and L. Zhou, *J. Mater. Chem. C* **12**, 16314 (2024).
- [20] J. Xie, L. Yan, J. Wang, G. Wang, Z. Sun, L. Zhou, J. Yang, and H. Dong, *Int. J. Hydrogen Energ.* **58**, 1587 (2024).
- [21] F. Mouhat and F.-X. Coudert, *Phys. Rev. B* **90**, 224104 (2014).
- [22] C. Lee, X. Wei, J. W. Kysar, and J. Hone, *Science* **321**, 385 (2008).
- [23] K. Hyeon-Deuk, A. B. Madrid, and O. V. Prezhdo, *Dalton Trans.* , 10069 (2009).
- [24] Q. Zheng, W. Chu, C. Zhao, L. Zhang, H. Guo, Y. Wang, X. Jiang, and J. Zhao, *Wiley Interdiscip. Rev.: Comput. Mol. Sci.* **9**, e1411 (2019).
- [25] H. Guo, W. Chu, Q. Zheng, and J. Zhao, *J. Phys. Chem. Lett.* **11**, 4662 (2020).
- [26] W. Li, J. Tang, D. Casanova, and O. V. Prezhdo, *ACS Energy Lett.* **3**, 2713 (2018).
- [27] L. Yan, A. Huang, B.-T. Wang, J.-G. Si, Y.-m. Ding, and L. Zhou, *Phys. Rev. B* **108**, 155309 (2023).
- [28] C.-F. Fu, Q. Zheng, X. Li, and J. Yang, *Nano Lett.* (2024).
- [29] W. Dou, Y. Jia, X. Hao, Q. Meng, J. Wu, S. Zhai, T. Li, W. Hu, B. Song, and M. Zhou, *J. Phys. Chem. Lett.* **12**, 2682 (2021).
- [30] H. Jin, T. Wang, Z.-R. Gong, C. Long, and Y. Dai, *Nanoscale* **10**, 19310 (2018).
- [31] D. Xiao, G.-B. Liu, W. Feng, X. Xu, and W. Yao, *Phys. Rev. Lett.* **108**, 196802 (2012).
- [32] H. Yuan, M. S. Bahramy, K. Morimoto, S. Wu, K. Nomura, B.-J. Yang, H. Shimotani, R. Suzuki, M. Toh, C. Kloc, *et al.*, *Nat. Phys.* **9**, 563 (2013).
- [33] J. R. Schaibley, H. Yu, G. Clark, P. Rivera, J. S. Ross, K. L. Seyler, W. Yao, and X. Xu, *Nat. Rev. Mater.* **1**, 1 (2016).
- [34] S. Li, W. Wu, X. Feng, S. Guan, W. Feng, Y. Yao, and S. A. Yang, *Phys. Rev. B* **102**, 235435 (2020).
- [35] S. Li, Q. Wang, C. Zhang, P. Guo, and S. A. Yang, *Phys. Rev. B* **104**, 085149 (2021).
- [36] L. Yan, J. Zhu, B.-T. Wang, P.-F. Liu, G. Wang, S. A. Yang, and L. Zhou, *Physical Review B* **107**, 085413 (2023).
- [37] Y. Ma, L. Kou, A. Du, B. Huang, Y. Dai, and T. Heine, *Phys. Rev. B* **97**, 035444 (2018).
- [38] M. K. Mohanta and A. De Sarkar, *Phys. Rev. B* **102**, 125414 (2020).
- [39] H. Din, M. Idrees, A. Albar, M. Shafiq, I. Ahmad, C. V. Nguyen, and B. Amin, *Phys. Rev. B* **100**, 165425 (2019).
- [40] Q. Yang, S. Zhang, C. Tan, H. Ye, X. Ming, S. Ingebrandt, and X. Chen, *J. Mater. Chem. C* **5**, 9412 (2017).
- [41] W. Yao, D. Xiao, and Q. Niu, *Phys. Rev. B* **77**, 235406 (2008).